



Numerical simulation for electron beam selective melting PBF additive manufacturing of molybdenum

Muhammad Qasim Zafar^{1,2} · Chaochao Wu^{1,2} · Haiyan Zhao^{1,2} · Du Kai^{2,3} · Qianming Gong^{2,3}

Received: 6 December 2020 / Accepted: 7 July 2021 / Published online: 9 August 2021

© The Author(s), under exclusive licence to Springer-Verlag London Ltd., part of Springer Nature 2021

Abstract

Molybdenum is a newly added material in additive manufacturing material cabinet, and it is under the spotlight owing to its crucial applications. The high-energy electron beam selective melting (EBSM) process is supposed to be a promising technique for molybdenum printing because of its vacuum environment. This paper presents EBSM numerical process simulation for molybdenum on macro- and mesoscale established with exclusive powder material modeling. Experimentally determined, process parameters are implemented in 3D macro- and 2D mesoscale models for a profound process insight. Primarily molybdenum powder material model is established, and a multi-track FEM simulation is performed to predict melt pool configuration, temperature field and phase transformation. Next, powder consolidation mechanism, side surface roughness, porosity, and voids are investigated through a CFD model, where the molybdenum particles are explicitly considered from the EBSM process viewpoint. Results proved the effectiveness of the numerical simulation for detailed EBSM process understanding for molybdenum material.

Keywords Additive manufacturing (AM) · Powder bed fusion (PBF) · Electron beam selective melting (EBSM) · Molybdenum material modeling · Finite element method (FEM) · Computational fluid dynamics (CFD)

1 Introduction

Additive manufacturing (AM) involves a layer-by-layer printing of 3D parts directly from a digital file as opposed to traditional manufacturing, and it is firmly moving towards another dimension [1, 2]. Additive manufacturing of refractory materials such as molybdenum and tungsten has become an attractive research domain, and significant development has been made so far [3–5]. The essential features of molybdenum

are strength and stability at elevated temperature, capability of solid solution strengthening, higher thermal conductivity, low coefficient of thermal expansion, thermal shock resistance, and greater stiffness. Molybdenum vessels are used in processing nuclear fuel pellets for high-temperature applications. Its high melting point makes it excellent for use as vapor deposition boats, hot forming dies, furnace parts, X-ray targets, thermocouples, and glass melting electrodes [6–8].

Additive manufacturing of pure molybdenum is not straightforward due to its exceptional thermal conductivity and excessive crack susceptibility[9]. Numerous attempts have been made with SLM technology to produce high-density crack-free molybdenum printings; nevertheless, in one way or the other, low fracture toughness, ductility, and greater oxygen affinity are supposed to be the dominant reasons for porosity and cracking in molybdenum [3, 5, 9]. Presumably, this issue may resolve in a vacuum environment in case of electron beam selective melting (EBSM) as the process is exclusively for conductive materials, and molybdenum is regarded as one of the highly conductive materials thus far [10]. The EBSM is preferred among PBF processes due to its adequate energy penetration, absorption efficacy, and higher build rates with a slight compromise on surface quality [11, 12]. The EBSM produces fine microstructure and better

✉ Haiyan Zhao
hyzhao@tsinghua.edu.cn

✉ Qianming Gong
gongqianming@tsinghua.edu.cn

¹ State Key Laboratory of Tribology, Department of Mechanical Engineering, Tsinghua University, Beijing 100084, People's Republic of China

² Key Laboratory of Advanced Materials Processing Technology, Ministry of Education, Tsinghua University, Beijing 100084, People's Republic of China

³ School of Material Science & Engineering, Tsinghua University, Beijing 100084, People's Republic of China

fatigue properties with low inception of residual stresses as compared to SLM which ultimately scale down crack susceptibility in fabrications [12, 13]. Since the process is integrated with a preheating module, primarily to avoid so-called smoke effect perhaps, it also contributes to better quality fabrications [14]. Notably, preheating is found to be favorable for better adhesion in direct energy deposition (DED) of molybdenum in recent work by John et al. [4]. Moreover, the EBSM process can print cobalt- and nickel-based superalloys, stainless and tool steels, invar, intermetallic compounds, aluminum, copper, niobium, and beryllium [15]. The fabrication of highly reflective, impurity sensitive, thermally superconductive, possessing elevated melting point materials as well as the capability of tailoring microstructure make EBSM additive manufacturing technique preeminent among others [12, 13, 16–18].

Since complex physical phenomena and rapid evolution of thermal behavior in the EBSM process are difficult to interpret experimentally perhaps, a numerical approach with experimental groundwork can adequately examine physical process, consolidation mechanism and dimensional accuracy of final part. Numerical simulation has been substantially involved in expediting the PBF process understanding and optimization contrary to the expensive traditional hit and trial scheme [19]. Multi-scale numerical simulation based on the process-structure-property relationship has become a way forward for design-predict-optimize in additive manufacturing. The combination of macro- and mesoscale simulation opened up new avenues to investigate the process physics and geometric inaccuracies [20, 21]. Yan et al. [22] proposed a multi-scale numerical scheme for efficient prediction of surface roughness, non-uniformity in melt tracks, and voids formation in PBF additive manufacturing.

Generally, on a macroscale, FEM simulation is performed by considering a continuum domain, and the discretized domain is calculated with partial differential equations in a finite element solver. It has been frequently implemented in additive manufacturing process optimization; particularly prediction of melt pool configuration, the evolution of process temperature, and geometric accuracy are the critical applications on a part scale. A pool of studies has shown the significance of FEM in the interpretation and optimization of the EBSM process [23–30]. However, additive manufacturing is more complex, and traditional constitutive equations involve in FEM solution may not provide a precise description of the physical process. Therefore, the simulation scale needs to be extended at meso-scale with a computation fluid dynamic (CFD) simulation to comprehend the EBSM process more accurately. It gives a more realistic temperature field and a better understanding of melt pool dynamics and process deficiencies perhaps with high computational cost. Typically, the CFD simulation involves a solution of nonlinear partial differential equations for mass, momentum, and energy conservation and broadly covers hydrodynamic effects such as balling, porosity, voids,

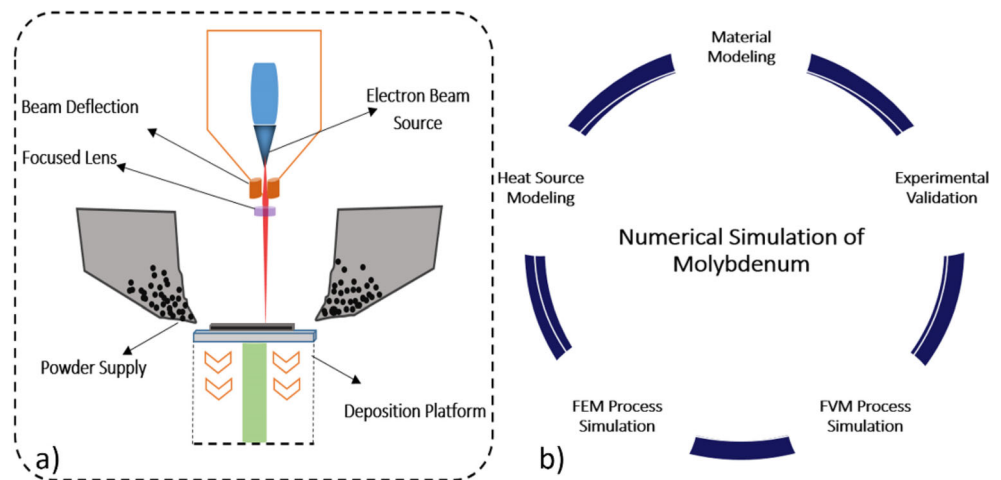
and surface roughness [31, 32]. For example, the “balling” effect is a serious concern in PBF process which is essentially due to insufficient fusion of substrate just below the deposited layer which deteriorates continuity of melt track. The FVM simulation work developed by Yan et al. [22] revealed that if the substrate under the melted particles is also melted, the melted particles will spread on the melted substrate to minimize the surface area which facilitates avoiding “balling” phenomena in consolidation. Similarly, another CFD simulation study was presented at the “Material Science Forum” to see the effect of energy input on surface morphology, and large surface roughness was attributed to low heat input for Ti6Al4V in EBSM additive manufacturing [33]. Numerical simulation exclusively for pure molybdenum is yet missing in CFD literature particularly from EBSM viewpoint [19, 31, 34, 35]. A coupled thermo-fluid model of molybdenum is developed for the analysis of the SLM process, processing parameters, melt pool dynamics, and defects using COMSOL®. However, instead of powder, bulk material properties of molybdenum were implemented in single track simulation [13]. Undoubtedly, numerical simulation on multiple lengths and time scales is an ideal tool to gain further insights and topological optimization for PBF additive manufacturing [13, 20, 36]. However, effective powder material modeling is very crucial to perform a meaningful simulation (Fig. 1) [37].

The proposed work is based on initial experiments of EBSM-PBF additive manufacturing for process parameter optimization and implementation of a numerical simulation scheme on macro- and mesoscale for detailed process insight for pure molybdenum. Primarily, molybdenum powder properties are established based on powder packing arrangement for numerical simulation. Then FEM simulation for multi-track EBSM process on as-built process parameters is accomplished to predict temperature field and melt pool morphology with ABAQUS® [51]. The molybdenum phase transformation from powder to the liquid and, subsequently, liquid to solid is exclusively considered. Furthermore, a 2D mesoscale multilayer CFD model is developed on as-built processing parameters using ANSYS (Fluent®) [53] for more in-depth process insight, specifically in terms of energy input, surface roughness, porosity, and void formation in EBSM printing. Thereafter, numerical simulation results are discussed for detailed process understanding at macro- and mesoscale. Finally, the article is concluded with a profound outlook for additive manufacturing and numerical simulation of molybdenum.

2 Electron beam selective melting

Arcam developed its first electron beam printer, and process involved selective melting of conductive powder through

Fig. 1 **a** EBSM process schematic. **b** Research paper scope



electron beam heat source, as instructed by a digital CAD file [38]. In a typical electron beam process, several electrons are emitted through an electrical heating filament and collide with powder particles to transfer energy because of elastic and inelastic collision [37]. The electron beam is handled with a set of magnetic lenses, and electrons are accelerated to a velocity of 0.1 and 0.4 times the speed of light [15]. The typical EBSM process involves four steps: primarily spreading a powder layer, then preheating with a defocused beam, after selectively melt powder particles with a focused beam, and finally lowering the platform equal to layer thickness as per illustration (Fig. 2a) [37]. The EBSM process operates under vacuum conditions up to the pressure of 10^{-3} Pa created by turbo-molecular pumps [15]. A small amount of helium is further introduced to ensure thermal stability during the process. The EBSM printer is equipped with a tungsten filament to obtain maximum beam power as 3KW with an acceleration voltage of 60kV along with a maximum electron beam current of 50mA. Generally, spherical molybdenum powder particles are utilized which is produced by gas atomization technology in the range of 40–90- μm particle size. The powder is stored in material hoppers, and powder particles are spread by moving racks on x, y plane in a layer scheme. A particular layer thickness is maintained by lowering the platform after consolidation of successive layers throughout the printing process. As-built processing parameters and melt pool sizes are scrutinized through a series of experiments. Final printing parameters are obtained through a comprehensive experimental trial using Q_{BEAM} Lab200 EBSM printer available at Tianjin Qingyan Zhi Shu Technology Co., Ltd China [40]. Experimental detail with relevant printing parameters is available in Table 1.

According to Qian et al. [41], energy density has a particular effect on melt pool geometry, and scan speed is another significant factor that controls melt pool size and ultimately affects surface morphology in the EBSM printing process [41]. Melt pool size and corresponding energy density are

obtained by implementing beam diameter equal to 200 μm [42]. The bulk energy density was adopted to evaluate the various combinations of parameters according to the following expression for the EBSM process.

$$Ev = \frac{UI}{e v s} \quad (1)$$

In the above expression, U , I , e , v , and s are the acceleration voltage, beam current, layer thickness, and scan speed, and s is line interval. Single-track molybdenum consolidation is obtained with the bulk energy density of 1200 J/mm³, and powder sintering is performed with a deflected beam before heating.

Single-track EBSM samples (Fig. 2b) were printed to obtain the optimized process parameter for molybdenum. Several set of parameters, e.g., scan speed, and beam current, were tried to selectively melt powder particles with subsequent energy density, and the corresponding melt pool size is observed. Melt pool width is approximated with wall thickness, and depth is measured up to the solidified powder bed in z -direction via single-track experiments. Quality printings are chosen through several inspection steps. First, printed fragments are removed from a molybdenum base plate, and properly consolidated printings are sorted out through visual inspection. Then selected chunks are further subjected to a detailed metallographic trial with optical electron microscopy, and distinct processing parameters are identified based on high-density solidified samples.

Once the optimum parameters are established from EBSM experiments of single track multilayer samples of molybdenum, then square specimens (15×15×10) were printed on optimized parameters to get maximum density in printed chunks. High-resolution X-ray computed tomography (CT) has been applied to measure relative density along with the spatial distribution, size, and shape of the pores in EBSM-printed parts. Previously, X-ray (CT) is successfully exercised for

Table 1 Experimental details for EBSM process parameter optimization for molybdenum printing

Exp No	Beam Current (mA)	Scan Speed (m/s)	Energy Density (J/mm ³)	Melt Pool Size (mm)	Exp No	Beam Power (mA)	Scan Speed (m/s)	Energy Density (J/mm ³)	Melt Pool Size (mm)
1	5		600	1.42	10	8		480	1.28
2	6		720	1.33	11	9		540	1.52
3	7		840	1.5	12	10		600	1.42
4	8		960	1.67	13	11	0.2	660	1.5
5	9	0.1	1080	1.18	14	12		720	1.56
6	10		1200	1.31	15	13		780	1.33
7	11		1320	1.52	16	11		440	1.15
8	12		1440	1.71	17	12	0.3	480	1.28
9	13		1560	1.65	18	13		520	1.19

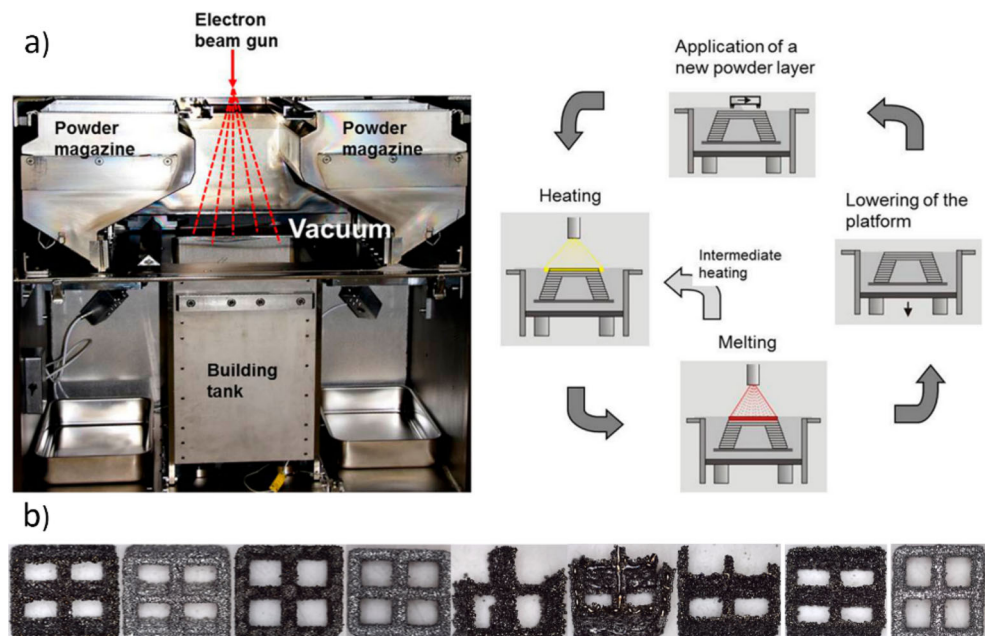
Ti6Al4V-printed parts in EBSM by Tamas-Williams et al. [43]. However, 99.99% density could only be achieved after recommended hot isostatic pressing (HIP) as post-treatment of EBSM printing parts [11]. The microstructure, grain morphology, and mechanical properties are further investigated for additively manufactured molybdenum samples. However, those investigations are beyond the scope of this study; perhaps printing parameters for molybdenum fabrication are exercised in macro- and mesoscale models for a comprehensive process understanding with exclusive material modeling, which is an obvious strength of the proposed study.

3 Numerical simulation

3.1 Material modeling

Powder properties are considerably different from their bulk, and temperature-dependent powder material properties play a crucial role in conductive numerical simulation. Initially, thermo-physical properties for solid molybdenum are taken from [13]. Powder density and thermal conductivity are calculated with a material modeling framework for electron beam process simulation proposed by Zafar MQ et al. [37].

Fig. 2 a Equipment details and a straightforward process sequence [39], b single-track multilayer molybdenum samples for process parameter optimization



3.1.1 Density

Powder density might influence other material properties such as conductivity and absorptivity of material, and it has a substantial effect on simulation quality. Previously powder densities for metallic material are treated as 40 to 60% of their bulk [37]. Gusarov et al. [44] and Tolochko et al. [45] concluded that the powder bed density might be dependent on their packing style in the powder bed. Likewise, SC, BCC, and FCC packing styles may have densities equal to 51.4%, 68%, and 74% of the bulk stated by Gusarov et al. [44]. Molybdenum powder density is taken as 68% of its bulk assuming BCC powder packing style in this numerical work.

$$\rho_{\text{powder}} = (1-\varphi)\rho_{\text{solid}} \quad (2)$$

where ρ and φ represent density and powder porosity, respectively. The proposed model is previously validated by Galati et al [46] for Ti6Al4V powder material in the EBSM context.

3.1.2 Thermal conductivity

Molybdenum thermal conductivity is calculated from conductivity model proposed by Tolochko et al. [45] (Fig. 3b), where conduction, convection, and radiation phenomena are estimated based on symmetric or random packing, as stated in [45].

$$\lambda_{\text{Powder}} = \lambda_r + \lambda_d + \lambda_c \quad (3)$$

$$\lambda_c \approx 0$$

In the above equation, λ_r represent thermal conductivity due to thermal radiation, and λ_d is the thermal conductivity due to conductive heat transfer via the adjacent necks of particles. Perhaps, thermal conductivity due to convection phenomena λ_c is overlooked due to vacuum conditions in the EBSM process.

Conductivity through radiation may be calculated as:

$$\lambda_r = \frac{16}{3} l \sigma T^3 \quad (4)$$

where l is the mean photon-free path between the scattering events, σ is the Stefan-Boltzmann constant, and T is the temperature. Tolochko et al. [45] assumed that l is equal to the particle diameter, whereas contact conductivity λ_d is proportional to the linear size of the contact between two particles [47].

$$\lambda_d = \Lambda \cdot \lambda_{\text{Solid}} \cdot r_c \quad \text{where } r_c = \frac{b}{r} \quad (5)$$

where r_c is thermal contact ratio and Λ is known as normalized contact thermal conductivity, and its value for BCC, SC, and Diamond powder packing is 1.732, 1.0, and 0.433, respectively [37]. Jamshidinia et al. [48] calculated normalized thermal conductivity based on random powder packing and took the r_c value 0.2 for Ti6Al4V; however, Gusarov et al. [44] assumed a contact ratio equal to 0.3 in his numerical model. Normalized contact thermal conductivity based on random powder packing along with a 0.25 contact size ratio is presumed for molybdenum powder in this study.

Since unrealistic heat gradient due to moving heat source may arise during the process; therefore, effective liquid conductivity is incorporated to stabilize the melt pool in process simulation. The Buoyancy and Marangoni effects are accounted with a so-called Bond number for convective heat transfer within the melt pool region. A bond number less than one represents Marangoni effect as dominant convection phenomena; however, greater than one speaks for the prevailing buoyancy effect.

$$Bo = \frac{\frac{\partial \rho}{\partial T} g L^2}{\frac{\partial \gamma}{\partial T}} \quad (6)$$

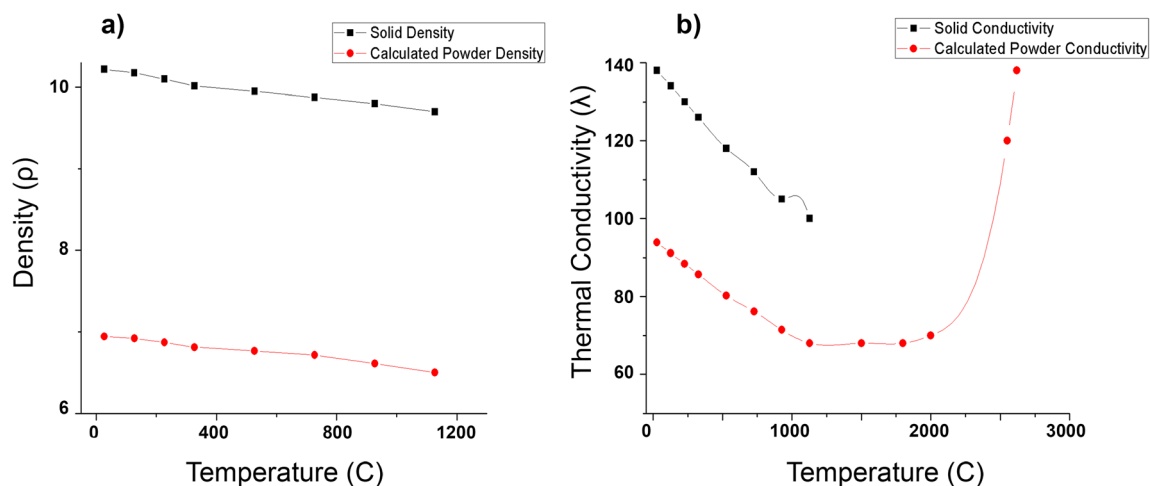


Fig. 3 Molybdenum powder material properties calculated from bulk: **a** powder density, **b** thermal conductivity

where $\frac{\partial \rho}{\partial T}$ and $\frac{\partial \gamma}{\partial T}$ are derivatives of density, and surface tension depends on temperature, g is acceleration, and L is the length of the system. The Marangoni effect is considered in the proposed study; however, the buoyant effect is overlooked due to lower bond number. Further detail is available in a recent publication [37].

Temperature-dependent thermal conductivity for powder is established through the above expressions, and liquid thermal conductivity of powder and solid is analogous above molybdenum melting point. Derived powder material properties are implemented in FEM and CFD model and the rest taken from [6] for this work.

3.2 Heat source modeling

One of the critical aspects in process simulation of PBF additive manufacturing is modeling of heat source to simulate heat input adequately on predefined pattern. The powder particles are supposed to be continuously melted with the movement of heat source and solidified along the scan track. The surface and the volumetric heat source can be chosen based on heat flux penetration in powder bed; usually volumetric heat source is implemented for the EBSM process [37]. A modified conical volumetric heat source with Gaussian intensity is employed along with a penetration function, to represent electron beam irradiation in 3D FE Model [49].

$$S(x, y, z) = f(z) \quad (7)$$

$$\frac{3\eta UI_b}{\pi \Phi_E^2} \exp \left\{ -\frac{3 \left[(x-x_s)^2 + (y-y_s)^2 \right]}{\Phi_E^2} \right\} \text{with } f(z)$$

$$= \frac{2}{h} \left(1 - \frac{z}{h} \right)$$

where S is the heat flux applied in a position with coordinate (x, y, z) , UI_b the energy of an electron beam, η the efficiency of the heat input, x_s, y_s the coordinate of beam center, Φ beam radius, and $f(z)$ penetration function.

Experimentally determined processing parameters, including electron beam radius, current, absorption, penetration, and movement, are steered through a user-subroutine DFLUX in FEM. The proposed 3D heat source is subsequently reduced to two-dimensional for CFD model by following a heat source derivation proposed by Korner et al. [50] for EBSM process simulation.

3.3 Finite element simulation

3.3.1 FEM model

A 3D finite element model is developed in ABAQUS® [51] with a single molybdenum powder layer ($15 \times 15 \times 0.1$ mm) on a solid molybdenum substrate (Fig. 4a). The substrate size is reduced to $20 \times 20 \times 5$ mm cross-section for topological

optimization. Thermo-physical properties for powder and solid molybdenum are assigned to corresponding sections. A tie constraint [52] was applied in the contact region of fused layer and substrate to bridge an effective heat and material phase transfer mechanism. Heat source and material phase transformation is realized through Fortran code, as a function of position and time.

3.3.2 Mesh scheme and preheat conditions

Simulation quality substantially depends on mesh; thus, a uniform meshing is applied on layer section, and a non-uniform coarse mesh is extended to the base plate with increasing density towards substrate tie surface. The proposed model is trialed with different mesh sizes, and corresponding results are compared to overcome discretization errors and to optimize computational time. Finally, a finer mesh size of $0.1 \times 0.1 \times 0.0333$ mm is implemented with 67500 elements for layer section and 6860 elements for the substrate. 8-node linear heat transfer brick (DC3D8) elements are picked for layer as well as for substrate to perform FEM thermal analysis. Since the EBSM process is relatively a hot powder bed fusion process and essentially a preheating step is introduced to sinter powder particles before melting. Therefore, substrate and layer elements are specified with an initial temperature to account preheating phenomenon in the FEM model. Predefined temperature conditions can be expressed as.

$$T(x, y, z, 0) = T_o \quad (8)$$

Initial temperature T_o values are assigned as 600°C and 1350°C for substrate and layer sections, respectively.

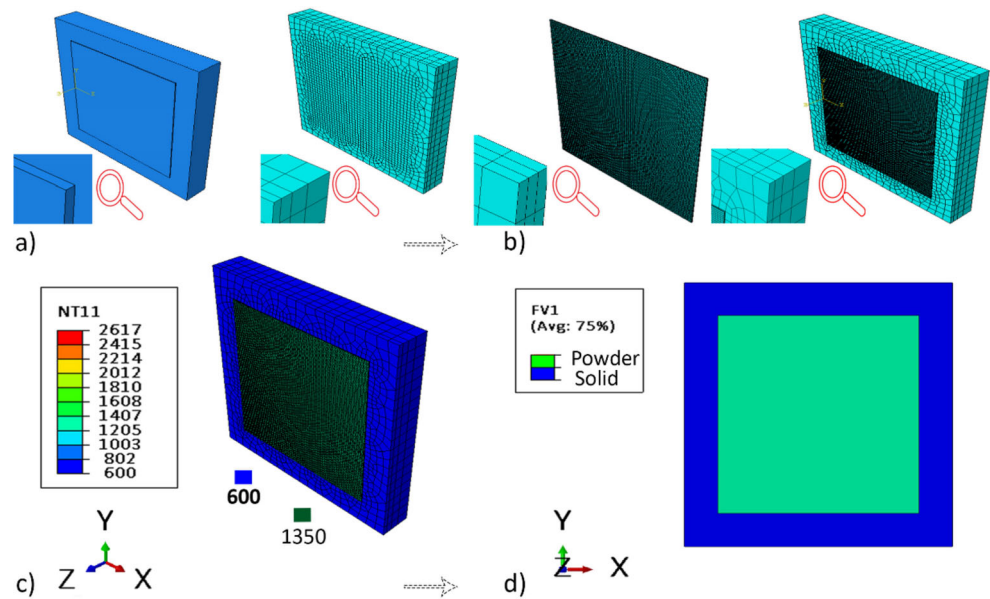
3.3.3 Material phase transformation

Essentially latent heat of fusion (dH) is considered for tracing phase transformation on each track during consolidation process in FEM simulation. It is envisaged through a user subroutine USDFLD coded in Fortran, and each phase is distinguished by a dedicated state variable. The state variables designated with the material state (powder, liquid, or solid) and subsequent material properties are switched to liquid and further turn to solid after the consolidation of powder in each track [25, 37].

$$dH = Cp dT \quad (9)$$

The frequent transition of heat source and subsequent phase transformation is controlled with a script in step time followed by a scan pattern, so that material properties for each phase could be switched accordingly for a more realistic simulation approach (Fig. 4d).

Fig. 4 **a** 3D FE model, **b** Mesh scheme for substrate and layer, **c** initial preheat boundary conditions, **d** phase transformation modeling.



3.3.4 Governing equations for FEM heat transfer analysis

A nonlinear transient heat transfer analysis is performed to simulate consolidating mechanism where general energy balance equation is represented as

$$Q_{total} = Q_{conduction} + Q_{radiation} + Q_{convection} \quad (10)$$

The governing heat conduction equation in a particular volume, according to Fourier's series, is

$$\begin{aligned} \frac{\partial}{\partial x} \left(\lambda_x \frac{\partial T}{\partial x} \right) + \frac{\partial}{\partial y} \left(\lambda_y \frac{\partial T}{\partial y} \right) + \frac{\partial}{\partial z} \left(\lambda_z \frac{\partial T}{\partial z} \right) + q \\ = \rho(T) C_p(T) \left(\frac{\partial T}{\partial t} \right) \end{aligned} \quad (11)$$

where, T , ρ , λ , q , c_p , and t are the temperature, material density, heat supplied rate, thermal conductivity, specific heat, and interaction time of the heat source and powder particles, respectively. The phase transformation is incorporated in FEM thermal analysis by considering enthalpy change. The above equation is modified to trace out phases and their corresponding material properties.

$$\begin{aligned} \frac{\partial}{\partial x} \left(\lambda_x \frac{\partial T}{\partial x} \right) + \frac{\partial}{\partial y} \left(\lambda_y \frac{\partial T}{\partial y} \right) + \frac{\partial}{\partial z} \left(\lambda_z \frac{\partial T}{\partial z} \right) + q \\ = \rho \frac{\partial H}{\partial t} \end{aligned} \quad (12)$$

Radiation heat loss is implemented on the substrate and layer top surface, according to Eq. 13.

$$Q = A \times \sigma \times \varepsilon \times (T^4 - T_a^4) \quad (13)$$

where ε , σ , T , T_a , and A are material emissivity, Stefan-Boltzmann constant, surface temperature, ambient temperature, and radiation surface area, respectively. The convection boundary condition is deliberately overlooked because of a vacuum processing condition in the EBSM printers. However, a heat dissipation boundary condition is implemented to compensate for the size of the substrate.

3.4 Mesoscale simulation

3.4.1 CFD model

A computationally efficient 2D powder scale CFD model is developed using ANSYS (Fluent®) [53] to study multilayer consolidation mechanism and melt pool morphology for molybdenum printing. The 2D calculation domain includes multiple powder layers, the solid material under the powder deposition, and the vacuum environment as per physical conditions. The proposed CFD model is an effort to interpret complex physical phenomena for selective melting of molybdenum, where powder particles are explicitly considered for prediction of melt pool morphology, side surface roughness, porosity, and voids.

3.4.2 Powder layer deposition

Usually, powder deposition and layer generation are accomplished through discrete element method or by using a free fall rain model in mesoscale simulation. The so-called rain model is preferred when it comes to achieving a desired packing density of a powder layer. Therefore, an integrated powder deposition model is developed to deposit powder particles in which required particle size and packing density could be

realized effectively. A profound algorithm for implemented powder deposition model is explained in the previous paper [34], whereas a user subroutine is developed for molybdenum powder deposition for this numerical simulation work [34]. The spherical powder particles with the typical log Gaussian distribution are considered, and powder layers are generated by using a free-fall process based on the following assumptions: (1) powder particles are spherical, (2) particles are considered geometrically, and the overlap of particles and mechanical forces are neglected, and (3) the individual particle moves along a random straight route until it came into contact with another particle or the wall. Essentially, the free fall process is a compressing process of powder, during which the packing density becomes higher and higher, especially if there is a vibration or periodical upside down [54, 55].

3.4.3 Computational fluid dynamic simulation

CFD simulation provides a deeper process insight by solving the governing partial differential equations of mass, momentum, and energy conservation. Energy input and analogous molten pool are driven by surface and volume forces. EBSM is investigated by solving Navier-Stokes equations. The powder molybdenum properties are implemented as per FEM model, and the rest of the fluid properties are taken from a previously published simulation study for CFD model [13]. It should be noted that process characteristics in multilayer processes are the prime focus of proposed work where material loss due to spatter or denudation phenomenon is overlooked for a bit of simplification. Molten pool is predominantly derived by surface tension, evaporation recoil pressure, gravity, buoyancy, etc. Fluid mechanics involved in additive manufacturing heat transfer is similar to welding; therefore, gravity and buoyancy may be regarded as negligible (Fig. 5).

The 2D computational domain comprises powder particles and a substrate. The minimum grid size is $5\mu\text{m} \times 5\mu\text{m}$, and the step time is 200ns to simulate multilayer single-track EBSM process. It is assumed that track length is long enough to give adequate process insight. Essentially 3 layers are simulated using optimum experimental parameters, and the cooling step

is incorporated in subsequent melting of layers to replicate physical process.

3.4.4 Governing equations for CFD analysis

CFD analysis generally solves the Navier-Stokes equation for a particular domain, and the entire process satisfies the following underlying conservation equations.

$$\frac{\partial(\rho)}{\partial t} + \nabla \cdot (\rho \vec{V}) = 0 \quad (14)$$

$$\frac{\partial(\rho \vec{v})}{\partial t} + \nabla \cdot (\rho \vec{v} \times \vec{v}) = \nabla \cdot (\mu \nabla \vec{v}) - \nabla p + S_{st} + A_{mush} \frac{(1-f_l)^2}{f_l^3 + \delta} \vec{v} \quad (15)$$

$$\frac{\partial}{\partial t}(\rho H) + \nabla \cdot (\rho \vec{V} H) = \nabla \cdot (\xi \nabla T) + Q_{input} \quad (16)$$

where S_{st} describes the momentum induced caused by surface tension. Q_{input} is the input heat source induced by an electron beam. The fourth term of the right-hand side in Eq. (15) is by frictional dissipation in the mushy zone. A_{mush} is the constant representing mushy zone morphology; δ the positive zero is used to avoid division by zero. f_l is the liquid fraction.

$$f_l = \begin{cases} 0 & T < T_{solidus} \\ \frac{T - T_{solidus}}{T_{liquidus} - T_{solidus}} & T_{solidus} < T < T_{liquidus} \\ 1 & T > T_{liquidus} \end{cases} \quad (17)$$

Since the EBSM process takes place in a vacuum, therefore, a description of a volume of fluid (VOF) model is incorporated in CFD simulation which distinguishes the computation domain in metal and high vacuum phases and volume denoted as F [34].

$$\frac{\partial F}{\partial t} + \vec{v} \cdot \nabla F = 0 \quad (18)$$

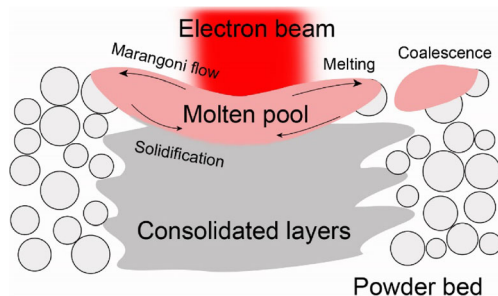


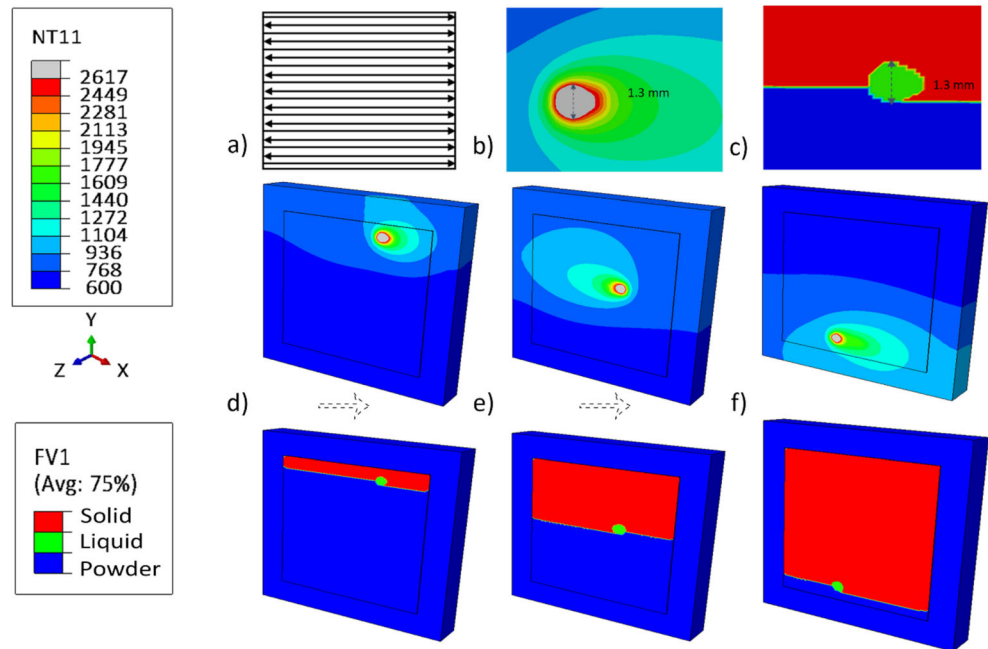
Fig. 5 EBSM consolidation mechanism on mesoscale [34]

4 Results and discussion

4.1 Macroscale simulation

Since the EBSM process is accomplished in a vacuum, it should be ensured that applied energy density is sufficient enough to melt and pierce in powder bed for adequate consolidation in a physical process. Thus far no appropriate technique is available to estimate temperature right on the layer for each track other than adopting a numerical scheme. FEM

Fig. 6 FEM thermal simulation. **a** Scan pattern. **b, c** Melt pool dimension. **d, e, f** Heat source movement with subsequent phase transformation at 0.5, 2.5, and 5 sec, respectively



heat transfer analysis is performed for a single-layer in the ABAQUS® standard [51]. A volumetric heat source with Gaussian distribution and material phase transformation is realized through user subroutines DFLUX and USDLFD, respectively [52]. A uniform bi-directional beam scan strategy is adopted in heating step to replicate Q_{BEAM} Lab 200 default printing scheme as demonstrated in Fig. 6a. Complete layer coalescence conceived on implemented energy density 1200 J/mm^3 for multi-track via phase transformation coupling in FEM simulation.

4.1.1 Heat source configuration

The heat source is implemented as a user-defined thermal load to provoke a localized heating phenomenon on the layer section. Next, it moves to trace scan pattern along with specific coordinates in every time increment (Fig. 6a). Subsequently, the confronted powder layer turns to liquid in a predefined shape when localized heat approaches the melting point of molybdenum. The peculiar molten pool gradually moves forward from a particular position with a specific velocity, and the previously melted region quickly solidifies. Temperature variation and corresponding melt pool size with its position on the x, y plane is recorded for each track during the consolidation of a single-layer as showed in Fig. 6b, c. There were negligible variations observed in melt pool configuration throughout the heating process. The heat source traveled on a predefined scan pattern and successfully melted the whole layer without interruption. It was observed that molten pool width is approximately equal to 1.3 mm and melt pool depth is almost 1.5 times of layer thickness which agrees well with single track EBSM experiments.

4.1.2 Phase transformation

Molybdenum phase transformation from powder to the liquid and subsequently liquid to solid is integrated through a subroutine USDLFD in FEM simulation to replicate the actual consolidation process [52]. A continuous melting and solidification phenomenon tracked in red color shows proper solidification of powder particles as a complete heating and phase transformation on a given set of processing parameters is illustrated in Fig. 6d, e, f. The heat source movement with specific scan velocity in predefined tracks is displayed to explain the entire process. Single-layer heating along with melt pool shape, size, heat penetration, and material phase transformation is observed at 0.5s, 2.5s, and 5, respectively. It is clear in phase transformation that solidification occurs when the temperature drops to its solidus temperature range because of the high cooling rate and rapid solidification velocity of molybdenum.

4.1.3 Multi-track temperature profile

The effectuated transient temperature field coupled with phase transformation gave a better process insight in multi-track thermal simulation (see Figs. 6 and 7). The transient temperature field is captured at 5 measured locations perpendicular to scan vector in the layer median. Heat source position and corresponding temperature curves for each point are traced in different colors as shown in Fig. 7. The relevant temperature curves start from preheating conditions and subsequent temperatures escalated beyond the melting point in the region of interest for each track. The highest peak reveals the instant temperature value in the melt pool vicinity, and gradually it

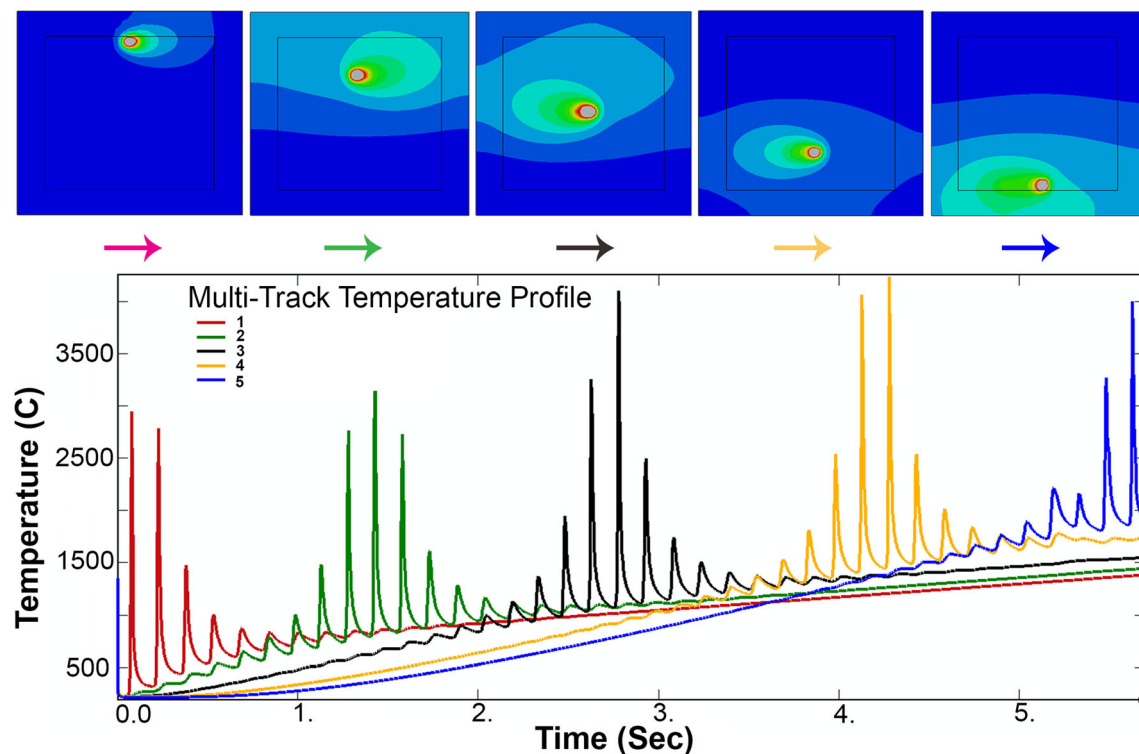


Fig. 7 Multi-track single-layer consolidation with temperature profile

dropped to heat-affected zone (HAZ) and thereafter layer surroundings. A gradual temperature increment is observed particularly from median to the end during melting; perhaps, this gradual temperature rise is due to accumulated heat gradient as a consequence of continuous heat flux input. Especially incremental temperature for 3rd and 4th curve is pretty much obvious; however, it slightly decreased later on transverse end. Presumably, this slight decrement is due to heat radiation and dissipation boundary conditions implemented on the substrate. However, melt pool dimensions do not fluctuate significantly in subsequent scan tracks in the entire heat transfer simulation process, which demonstrates a favorable agreement with EBSM experimental conditions.

Unrealistic temperature due to increasing thermal gradient is hindered by liquid thermal conductivity in the melt pool which effectively controls the outstripping of temperature peaks for each track. Consequently, a relatively uniform melt pool configuration is established throughout the heat transfer analysis.

4.2 Mesoscale simulation

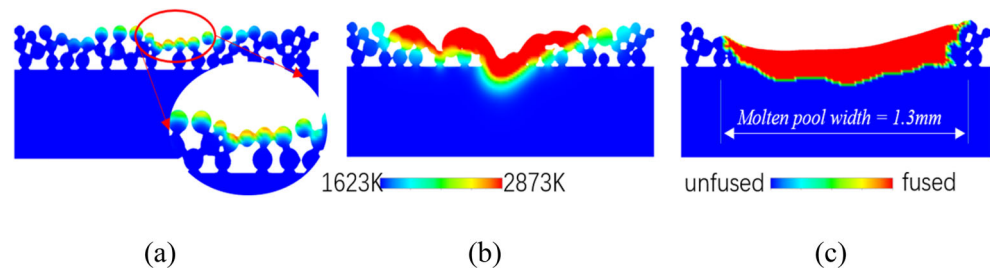
Single-track results calculated by a 2D mesoscale model with an in-plane moving heat source (at optimum parameters) determined the behavior of the molten pool and the printing quality. Especially, side roughness is a key concern as interior surfaces of printed chunks are difficult to grind or polish. Primarily, simulation results for powder behavior during heat

evolution, melting, solidification, surface roughness, and void formation are discussed in this section.

4.2.1 Powder behavior

When a localized accelerated electron beam irradiates powder particles, heat penetrates from the surface to a certain depth in a powder bed. Consequently, it provokes complex heat and mass transportation phenomena during the selective melting of powder. Electron beam interaction with powder particles and subsequent heat evolution process is demonstrated in Fig. 8a. Magnified view shows that molybdenum particles started to consolidate right on substrate followed by so-called necking phenomena during interaction with high energy electrons. Subsequently, Fig. 8b illuminates the coalescence of melting particles predominantly stimulated by surface tension. Finally, Fig. 8c substantiated a melt track formation after solidification along with partially consolidated powder particles adhering to the solidified walls. The sticking particles contribute to the side surface roughness and would affect melt pool dynamics. When the electron beam starts coalescence in the powder bed, then in contact particles may tend to displace in the track vicinity predominantly by surface tension. Normally, molten pool displacement emerges from low to high powder packing density in the PBF process, which may cause heat and mass transportation in a lateral direction, which contributes to maintaining molten pool configuration. The calculated molten pool width is 1.3mm (Fig. 8c), which validates the experimental

Fig. 8 Thermal process of powder in single track EBSM: **a** heating, **b** coalescence and liquid flow, **c** solidification, and the resultant melt pool width



results stated earlier. Moreover, individual powder particles in a layer are completely melted on optimum processing parameters based on input energy density.

4.2.2 Prediction of surface roughness

Essentially, the side roughness is rolled out due to insufficient melting of powder particles in a melt track; therefore, the influence of heat input on surface roughness in a multilayer consolidation process is visualized through CFD simulation. Two cases were calculated with different heat inputs, and subsequent solidified tracks are examined to analyze side roughness. Mesoscale simulation results demonstrated the efficacy of the established model for adequate prediction of side roughness as shown in Fig. 9a, b. It is observed that low energy density leads to a more asymmetrical fusion zone between layer and substrate and eventually leads to “balling” formation and discontinuous melt track which yield higher roughness (see Fig. 9c, d). Perhaps, a substantial energy input could increase coalescence of powder particles and establish a proper fusion zone with a substrate to avoiding so-called “balling” phenomena [22]. Conclusively, the energy density adopted in this simulation melted the powder particles completely in subsequent layers and maintained a specified melt pool configuration in each track as per the experimental trial.

Numerical simulation for 2D molybdenum cross-section provided an adequate process understanding for roughness prediction in the multilayer EBSM process (Fig. 9).

4.2.3 Porosity and voids

The void formation is mainly due to lack of fusion because of insufficient heat input or mass loss for some quickly evaporated metals [22]. The heat input consequence for molybdenum powder is evaluated with an out-of-plane moving heat source to observe melting, consolidation, porosity, and void formation (Fig. 10). The solidified height increases with the consolidation of several powder layers (Fig. 10a, c, e). If the input energy density does not penetrate up to the preceding layers, then there might be porosity, and void formation happens between subsequent layers as shown in Fig. 10f. While with higher heat input, this situation could be eliminated to a satisfactory level. Overestimation of heat input could lead to keyhole formation in final printings, and a single-layer case is feasible for estimation of heat input for actual layer thickness as shown earlier in Fig. 8c. The actual layer height used in the simulation is estimated by nominal layer thickness over powder packing density. However, for more realistic results, several layers are indispensable for porosity and voids evaluation in subsequent layers with mesoscale simulation.

Porosity and voids can be seen in magnified view (Fig. 10f) which is caused by insufficient heat penetration in powder layers. The proposed numerical simulation with a multilayer CFD model could investigate the powder behavior, surface quality, and void formation mechanism. Although interlayer bonding is quite favorable, however, some variations may be possible when it comes to experimental validation. This comes from the stochastic nature of powder particle

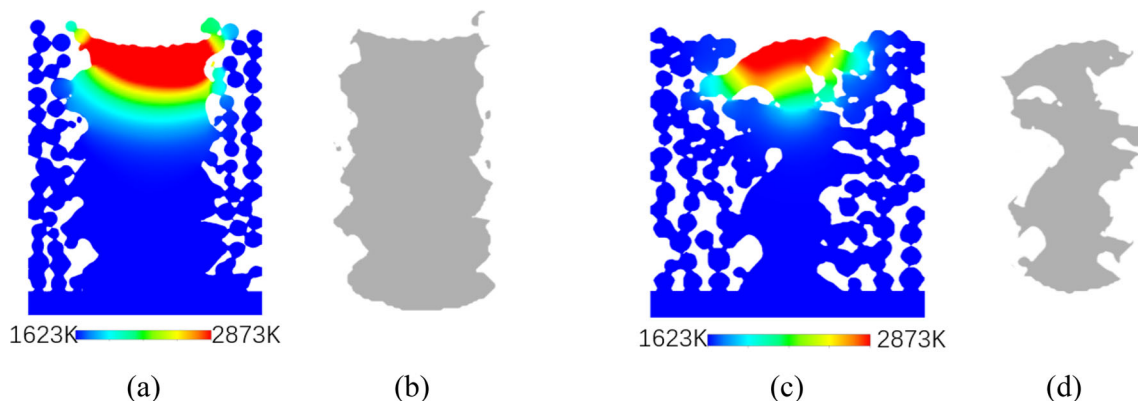
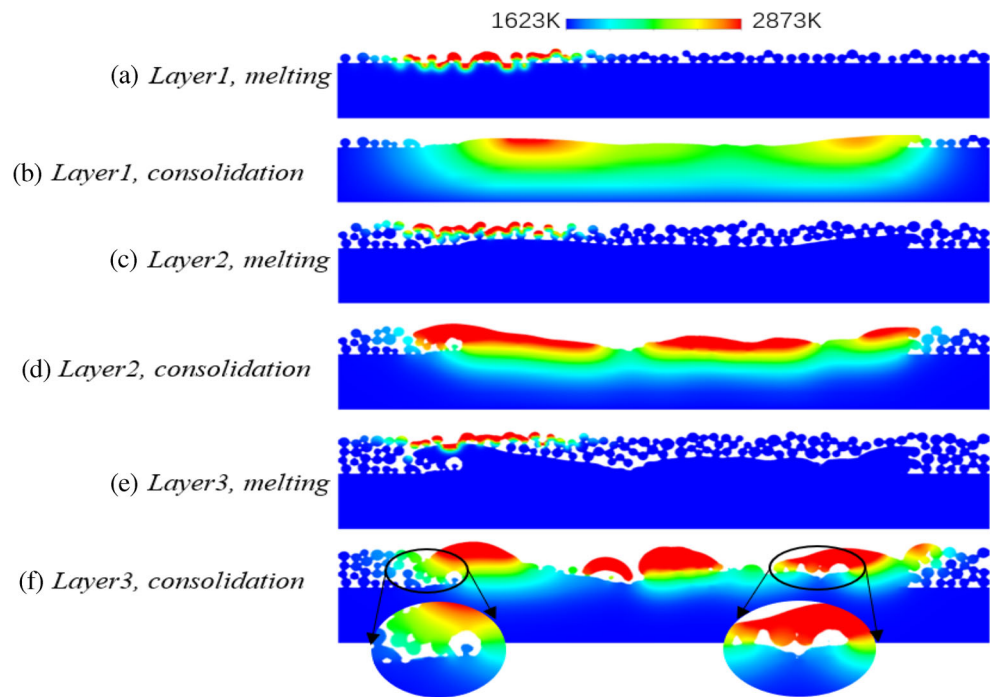


Fig. 9 Simulation results of a thin wall cross-section with different heat inputs: **a** temperature profile and **b** fused zone of high heat input, **c** temperature profile, and **d** fused zone of low heat input

Fig. 10 Void formation during multilayer EBSM process followed by melting and consolidation of subsequent layers



distribution as size and subsequent particle position would never match with the actual printing process. Perhaps, it may have a slight influence, which can be overlooked and might not confine the significance of the proposed model.

5 Conclusion and outlook

This work is based on numerical simulation implemented for comprehensive thermal investigation in EBSM powder bed fusion additive manufacturing on macro- and mesoscale followed by experiments. Powder material modeling for molybdenum is primarily established for numerical simulation. Then a single-layer multi-track 3D FEM simulation is performed based on experimentally determined processing parameters. Further, a powder-scale CFD model is developed to probe the melt pool morphology and powder consolidation mechanism for printing quality and intra-layer void formation. The FEM and CFD model is validated by comparing the energy density and relevant molten pool size from experimental results. It is concluded that FEM and FVM modeling and simulation have the potential to look into process physics, and it can effectively complete the design-predict-optimize cycle in additive manufacturing even if a new material is under observation.

FEM simulation has estimated the temperature evolution in conjunction with phase transformation during the multi-track EBSM process. The FEM simulation results show the temperature profile with the highest temperature peak for each track. It is concluded that heat input in the form of energy density consolidated each track adequately as the peak temperature

exceeding the melting point perhaps, owing to liquid conductivity, the temperature gradient does not outstrip during the process. Phase transformation illustrated that powder particles are completely consolidated under the selected parameters by maintaining the heat source dimensions.

Multilayer thin wall CFD simulation results revealed that 1200 J/mm^3 heat input is sufficient to consolidate pore-free solid tracks. Especially track width and depth are analogous to corresponding experimental results, and it can reduce the side roughness by proper melting and solidification in subsequent powder layers. The side roughness increased because of track fluctuation stimulated by the coalescence of particles and unevenness of powder distribution. For porosity elimination, actual layer height should be accounted to ensure adequate energy input that can sufficiently melt powder particles and reduce void formation.

The proposed work on macro- and mesoscale numerical simulation can examine, predict, and optimize the EBSM process for molybdenum effectively. It would be extended to a more comprehensive multilayer and multi-track 3D numerical simulation work for performance evaluation of molybdenum printing in the future.

Acknowledgements The principal author would like to extend his gratitude to Prof. Ghulam Hussain and Ghulam Ishaq Khan Institute of Engineering Science & Technology, Topi, Pakistan, for visiting scholar position during pandemic outbreak.

Author contribution Muhammad Qasim Zafar: Molybdenum material modeling, FEM simulation, and writing/revision/proofreading—original

draft. Chaochao Wu: mesoscale simulation and writing. Prof. Haiyan Zhao: supervision, resources, and review. Du Kai: EBSM experiments. Prof. Qianming Gong: experiments and supervision.

Funding This work is supported by the funding of the National Key R&D Program of China (2017YFB1103300), State Key Lab of Tribology, Tsinghua University China (SKLT2018B06), and National Natural Science Foundation of China (51975320).

Data availability The simulation data may not be available.

Declarations

Ethical approval It is to affirm that all the authors enlisted in this manuscript have agreed for authorship and sequence of authorship, and they read and approved the manuscript for submission.

Competing interests The authors declare no competing interests.

References

- Rajaguru K, Karthikeyan T, Vijayan V (2020) Additive manufacturing – State of art. *Materials Today: Proceedings* 21: 628–633. <https://doi.org/10.1016/j.matpr.2019.06.728>
- Zafar MQ, Zhao H (2020) 4D printing: future insight in additive manufacturing. *Met Mater Int* 26:564–585. <https://doi.org/10.1007/s12540-019-00441-w>
- Faidel D, Jonas D, Natour G, Behr W (2015) Investigation of the selective laser melting process with molybdenum powder. *Addit Manuf* 8:88–94. <https://doi.org/10.1016/j.addma.2015.09.002>
- Johnson JL, Palmer T (2019) Directed energy deposition of molybdenum. *Int J Refract Met Hard Mater* 84:105029. <https://doi.org/10.1016/j.jrmhm.2019.105029>
- Braun J, Kaserer L, Stajkovic J, Leitz KH, Tabernig B, Singer P, Leibenguth P, Gspan C, Kestler H, Leichtfried G (2019) Molybdenum and tungsten manufactured by selective laser melting: analysis of defect structure and solidification mechanisms. *Int J Refract Met Hard Mater* 84:104999. <https://doi.org/10.1016/j.jrmhm.2019.104999>
- SE P Molybdenum. The all-rounder among the specialists. <https://www.plansee.com/en/materials/molybdenum.html>
- Ciulik J, Shields JA, Kumar P., Leonhardt T., Johnson JL (2015) Properties and selection of PM refractory metals. In: *ASM Handbook Vol.7, Powder Technologies and Application*. ASM International, Materials Park, OH, pp 594–598
- Shields J (2013) Applications of molybdenum metal and its alloys. *Int Molybdenum Assoc*. ISBN 978-1-907470-30-1
- Wang D, Yu C, Ma J, Liu W, Shen Z (2017) Densification and crack suppression in selective laser melting of pure molybdenum. *Mater Des* 129:44–52. <https://doi.org/10.1016/j.matdes.2017.04.094>
- Kolarikova M, Kolarik L, Vondrouš P (2012) Welding of thin molybdenum sheets by EBW and GTAW. In: *23rd DAAAM International Symposium on Intelligent Manufacturing and Automation 2012*. pp 1005–1008
- Gong X, Anderson T, Chou K (2014) Review on powder - based electron beam additive manufacturing technology. *Manuf Rev* 1:1–9. <https://doi.org/10.1051/mfreview/2014001>
- Murr LE, Gaytan SM (2014) 10.06 - Electron beam melting. In: *Saleem H, Gilmar FB, Chester J VT, Bekir Y (eds) Comprehensive materials processing*. Elsevier, pp 135–161 <https://doi.org/10.1016/B978-0-08-096532-1.01004-9>
- Leitz KH, Grohs C, Singer P, Tabernig B, Plankensteiner A, Kestler H, Sigl LS (2018) Fundamental analysis of the influence of powder characteristics in selective laser melting of molybdenum based on a multi-physical simulation model. *Int J Refract Met Hard Mater* 72: 1–8. <https://doi.org/10.1016/j.jrmhm.2017.11.034>
- Leung CLA, Tosi R, Muzangaza E, Nonni S, Withers PJ, Lee PD (2019) Effect of preheating on the thermal, microstructural and mechanical properties of selective electron beam melted Ti-6Al-4V components. *Mater Des* 174:107792. <https://doi.org/10.1016/j.matdes.2019.107792>
- Galati M, Iuliano L (2018) A literature review of powder-based electron beam melting focusing on numerical simulations. *Addit Manuf* 19:1–20. <https://doi.org/10.1016/j.addma.2017.11.001>
- Körner C, Helmer H, Bauereiß A, Singer RF (2014) Tailoring the grain structure of IN718 during selective electron beam melting. In: *MATEC Web of Conferences*. <https://doi.org/10.1051/mateconf/20141408001>
- Murr LE, Li S (2016) Electron-beam additive manufacturing of high-temperature metals. *MRS Bull* 41:752–757
- Konyashin I, Hinnens H, Ries B, Kirchner A, Klöden B, Kieback B, Nilen RWN, Sidorenko D (2019) Additive manufacturing of WC-13%Co by selective electron beam melting: achievements and challenges. *Int J Refract Met Hard Mater* 84:105028. <https://doi.org/10.1016/j.jrmhm.2019.105028>
- Francois MM, Sun A, King WE, Henson NJ, Tourret D, Bronkhorst CA, Carlson NN, Newman CK, Haut T, Bakosi J, Gibbs JW, Livescu V, Vander Wiel SA, Clarke AJ, Schraad MW, Blacker T, Lim H, Rodgers T, Owen S, Abdeljawad F, Madison J, Anderson AT, Fattebert JL, Ferencz RM, Hodge NE, Khairallah SA, Walton O (2017) Modeling of additive manufacturing processes for metals: challenges and opportunities. *Curr Opin Solid State Mater Sci* 21: 198–206. <https://doi.org/10.1016/j.cossms.2016.12.001>
- Hashemi SM, Parvizi S, Baghbanjavahid H, Tan ATL, Nematollahi M, Ramazani A, Fang NX, Elahinia M (2021) Computational modelling of process–structure–property–performance relationships in metal additive manufacturing: a review. *Int Mater Rev*. <https://doi.org/10.1080/09506608.2020.1868889>
- Yan W, Lin S, Kafka OL et al (2018) Modeling process-structure-property relationships for additive manufacturing. *Front Mech Eng* 13:482–492. <https://doi.org/10.1007/s11465-018-0505-y>
- Yan W, Ge W, Qian Y, Lin S, Zhou B, Liu WK, Lin F, Wagner GJ (2017) Multi-physics modeling of single/multiple-track defect mechanisms in electron beam selective melting. *Acta Mater* 134: 324–333. <https://doi.org/10.1016/j.actamat.2017.05.061>
- Qi HB, Yan YN, Lin F, Zhang RJ (2007) Scanning method of filling lines in electron beam selective melting. *Proc Inst Mech Eng Part B J Eng Manuf* 221:1685–1694. <https://doi.org/10.1243/09544054JEM913>
- Zäh MF, Lutzmann S (2010) Modelling and simulation of electron beam melting. *Prod Eng* 4:15–23. <https://doi.org/10.1007/s11740-009-0197-6>
- Cheng B, Chou K (2013) Melt pool geometry simulations for powder-based electron beam additive manufacturing. In: *24th International SFF Symposium - An Additive Manufacturing Conference, SFF 2013*
- Wang X, Gong X, Chou K (2015) Scanning speed effect on mechanical properties of Ti-6Al-4V alloy processed by electron beam additive manufacturing. *Procedia Manufacturing* 1:287–295. <https://doi.org/10.1016/j.promfg.2015.09.026>
- Shen N, Chou K (2012) Numerical thermal analysis in electron beam additive manufacturing with preheating effects. In: *23rd Annual International Solid Freeform Fabrication Symposium - An Additive Manufacturing Conference, SFF 2012*
- Riedlbauer D, Scharowsky T, Singer RF, Steinmann P, Körner C, Mergheim J (2017) Macroscopic simulation and experimental measurement of melt pool characteristics in selective electron beam

- melting of Ti-6Al-4V. *Int J Adv Manuf Technol* 88:1309–1317. <https://doi.org/10.1007/s00170-016-8819-6>
29. Gong X, Cheng B, Price S, Chou K (2013) Powder-bed electron-beam-melting additive manufacturing: powder characterization, process simulation and metrology. *Early Career Tech Conf Birmingham, AL*
 30. Cheng B, Price S, Lydon J, Cooper K, Chou K (2014) On process temperature in powder-bed electron beam additive manufacturing: model development and validation. *J Manuf Sci Eng* 136. <https://doi.org/10.1115/1.4028484>
 31. Khairallah SA, Anderson AT, Rubenchik A, King WE (2016) Laser powder-bed fusion additive manufacturing: physics of complex melt flow and formation mechanisms of pores, spatter, and denudation zones. *Acta Mater* 108:36–45. <https://doi.org/10.1016/j.actamat.2016.02.014>
 32. Körner C, Attar E, Heintz P (2011) Mesoscopic simulation of selective beam melting processes. *J Mater Process Technol* 211:978–987. <https://doi.org/10.1016/j.jmatprotec.2010.12.016>
 33. Wu C, Zafar MQ, Zhao H (2021) Investigation on surface roughness in electron beam selective melting by mesoscale model. *Mater Sci Forum* 1016 MSF:1630–1635. <https://doi.org/10.4028/www.scientific.net/MSF.1016.1630>
 34. Wu C, Zafar MQ, Zhao H (2021) Numerical investigation of consolidation mechanism in powder bed fusion considering layer characteristics during multilayer process. *Int J Adv Manuf Technol* 113: 2087–2100. <https://doi.org/10.1007/s00170-021-06768-2>
 35. Jamshidinia M, Kong F, Kovacevic R (2013) The Coupled CFD-FEM Model of Electron Beam Melting® (EBM). <https://doi.org/10.13140/2.1.4136.2245>
 36. Markl M, Körner C (2016) Multiscale modeling of powder bed-based additive manufacturing. *Annu Rev Mater Res* 46:93–123. <https://doi.org/10.1146/annurev-matsci-070115-032158>
 37. Zafar MQ, Wu CC, Zhao H, Wang J, Hu X (2020) Finite element framework for electron beam melting process simulation. *Int J Adv Manuf Technol* 109:2095–2112
 38. Arcam (2016) JUST ADD: Arcam – the innovative leader in additive manufacturing solutions for the production of orthopedic implants and aerospace components. 19
 39. Körner C (2016) Additive manufacturing of metallic components by selective electron beam melting - a review. *Int Mater Rev* 61: 361–377. <https://doi.org/10.1080/09506608.2016.1176289>
 40. Tianjin Qingyan Zhi Shu Technology Co., Ltd China. en.qbeam-3d.com
 41. Qian Y, Yan W, Lin F (2018) Parametric study and surface morphology analysis of electron beam selective melting. *Rapid Prototyp J* 24:1586–1598. <https://doi.org/10.1108/RPJ-05-2017-0088>
 42. Guo C, Lin F, Ge W (2014) Study on the fabrication process of 316L stainless steel via electron beam selective melting. *Jixie Gongcheng Xuebao/Journal Mech Eng* 50:152. <https://doi.org/10.3901/JME.2014.21.152>
 43. Tammas-Williams S, Zhao H, Léonard F, Derguti F, Todd I, Prangnell PB (2015) XCT analysis of the influence of melt strategies on defect population in Ti-6Al-4V components manufactured by selective electron beam melting. *Mater Charact* 102:47–61. <https://doi.org/10.1016/j.matchar.2015.02.008>
 44. Gusarov AV, Laoui T, Froyen L, Titov VI (2003) Contact thermal conductivity of a powder bed in selective laser sintering. *Int J Heat Mass Transf* 46:1103–1109. [https://doi.org/10.1016/S0017-9310\(02\)00370-8](https://doi.org/10.1016/S0017-9310(02)00370-8)
 45. Tolochko NK, Arshinov MK, Gusarov AV, Titov VI, Laoui T, Froyen L (2003) Mechanisms of selective laser sintering and heat transfer in Ti powder. *Rapid Prototyp J* 9:314–326. <https://doi.org/10.1108/13552540310502211>
 46. Galati M, Snis A, Iuliano L (2019) Powder bed properties modeling and 3D thermo-mechanical simulation of the additive manufacturing Electron Beam Melting process. *Addit Manuf* 30: 100897. <https://doi.org/10.1016/j.addma.2019.100897>
 47. Raiser Z (1967) Physics of shock waves and high-temperature hydrodynamic phenomena. Academic Press, New York, NY
 48. Jamshidinia M, Kong F, Kovacevic R (2013) Numerical Modeling of Heat Distribution in the Electron Beam Melting ® of Ti-6Al-4V. *J Manuf Sci Eng* 135. <https://doi.org/10.1115/1.4025746>
 49. Shen N, Chou K (2012) Thermal modeling of electron beam additive manufacturing process: powder sintering effects. In: ASME 2012 International Manufacturing Science and Engineering Conference. p 287
 50. Körner C, Bauereiß A, Attar E (2013) Fundamental consolidation mechanisms during selective beam melting of powders. *Model Simul Mater Sci Eng* 21:085011. <https://doi.org/10.1088/0965-0393/21/8/085011>
 51. Hibbitt Karlsson, Sorensen (2004) Abaqus Analysis... - Google Scholar. https://scholar.google.com/scholar?hl=en&as_sdt=0,5&q=Hibbitt,+Karlsson,+Sorensen,+2004.+Abaqus+Analysis+Users+Manual,+25.2.3+Dflux.+Abaqus,+Inc. Accessed 29 May 2021
 52. (2018) ABAQUS 2018 Documentation, Dassault Systèmes, Providence (USA)
 53. Inc ANSYS (2013) ANSYS FLUENT Theory Guide. Release 182: 21–29. [https://doi.org/10.1016/0140-3664\(87\)90311-2](https://doi.org/10.1016/0140-3664(87)90311-2)
 54. Markl M, Körner C (2018) Powder layer deposition algorithm for additive manufacturing simulations. *Powder Technol* 330:125–136. <https://doi.org/10.1016/j.powtec.2018.02.026>
 55. Lee YS, Nandwana P, Zhang W (2018) Dynamic simulation of powder packing structure for powder bed additive manufacturing. *Int J Adv Manuf Technol* 96:1507–1520. <https://doi.org/10.1007/s00170-018-1697-3>

Publisher's note Springer Nature remains neutral with regard to jurisdictional claims in published maps and institutional affiliations.

Terms and Conditions

Springer Nature journal content, brought to you courtesy of Springer Nature Customer Service Center GmbH (“Springer Nature”).

Springer Nature supports a reasonable amount of sharing of research papers by authors, subscribers and authorised users (“Users”), for small-scale personal, non-commercial use provided that all copyright, trade and service marks and other proprietary notices are maintained. By accessing, sharing, receiving or otherwise using the Springer Nature journal content you agree to these terms of use (“Terms”). For these purposes, Springer Nature considers academic use (by researchers and students) to be non-commercial.

These Terms are supplementary and will apply in addition to any applicable website terms and conditions, a relevant site licence or a personal subscription. These Terms will prevail over any conflict or ambiguity with regards to the relevant terms, a site licence or a personal subscription (to the extent of the conflict or ambiguity only). For Creative Commons-licensed articles, the terms of the Creative Commons license used will apply.

We collect and use personal data to provide access to the Springer Nature journal content. We may also use these personal data internally within ResearchGate and Springer Nature and as agreed share it, in an anonymised way, for purposes of tracking, analysis and reporting. We will not otherwise disclose your personal data outside the ResearchGate or the Springer Nature group of companies unless we have your permission as detailed in the Privacy Policy.

While Users may use the Springer Nature journal content for small scale, personal non-commercial use, it is important to note that Users may not:

1. use such content for the purpose of providing other users with access on a regular or large scale basis or as a means to circumvent access control;
2. use such content where to do so would be considered a criminal or statutory offence in any jurisdiction, or gives rise to civil liability, or is otherwise unlawful;
3. falsely or misleadingly imply or suggest endorsement, approval, sponsorship, or association unless explicitly agreed to by Springer Nature in writing;
4. use bots or other automated methods to access the content or redirect messages
5. override any security feature or exclusionary protocol; or
6. share the content in order to create substitute for Springer Nature products or services or a systematic database of Springer Nature journal content.

In line with the restriction against commercial use, Springer Nature does not permit the creation of a product or service that creates revenue, royalties, rent or income from our content or its inclusion as part of a paid for service or for other commercial gain. Springer Nature journal content cannot be used for inter-library loans and librarians may not upload Springer Nature journal content on a large scale into their, or any other, institutional repository.

These terms of use are reviewed regularly and may be amended at any time. Springer Nature is not obligated to publish any information or content on this website and may remove it or features or functionality at our sole discretion, at any time with or without notice. Springer Nature may revoke this licence to you at any time and remove access to any copies of the Springer Nature journal content which have been saved.

To the fullest extent permitted by law, Springer Nature makes no warranties, representations or guarantees to Users, either express or implied with respect to the Springer nature journal content and all parties disclaim and waive any implied warranties or warranties imposed by law, including merchantability or fitness for any particular purpose.

Please note that these rights do not automatically extend to content, data or other material published by Springer Nature that may be licensed from third parties.

If you would like to use or distribute our Springer Nature journal content to a wider audience or on a regular basis or in any other manner not expressly permitted by these Terms, please contact Springer Nature at

onlineservice@springernature.com